

Over 13% Efficient, Ambient Air-Processed $\text{CuIn}(\text{S},\text{Se})_2$ Solar Cells via Compositional Engineering of Molecular Inks

Sunil Suresh, Daniel Abou-Ras, Towhid H. Chowdhury, and Alexander R. Uhl*

A dimethylformamide (DMF) and thiourea (TU)-based ink deposition route is used to fabricate narrow bandgap (≈ 1.0 eV) $\text{CuIn}(\text{S},\text{Se})_2$ (CISSe) films with Cu-poor ($[\text{Cu}]/[\text{In}] = 0.85$), stoichiometric ($[\text{Cu}]/[\text{In}] = 1.0$), and Cu-rich ($[\text{Cu}]/[\text{In}] = 1.15$) compositions for photovoltaic applications. Characterization of KCN- or $(\text{NH}_4)_2\text{S}$ -treated Cu-rich absorber films using X-ray diffraction and scanning electron microscopy confirms the removal of copper-selenide phases from the film surface, while electron backscatter diffraction measurements and depth-dependent energy-dispersive X-ray spectroscopy indicate remnant copper-selenides in the absorber layer bulk. Contrary to best practice for vacuum-processed cells, optimum $[\text{Cu}]/[\text{In}]$ ratios appear to be stoichiometric, rather than Cu-poor, in DMF–TU-based CISSe devices. Accordingly, stoichiometric film compositions yield large-grained (≈ 2 μm) absorber layers with smooth absorber surfaces (root mean square roughness < 20 nm) and active area device efficiencies of 13.2% (without antireflective coating). Notably, these devices reach 70.0% of the Shockley–Queisser limit open-circuit voltage (i.e., 526 mV at E_g of 1.01 eV), which is among the highest for ink-based CISSe devices.

PCEs ($> 25.0\%$) can be achieved by 2-terminal tandem devices when the bandgaps of the top and bottom films are about ≈ 1.6 and 0.94 eV, respectively.^[3] For the bottom cell, low-bandgap $\text{CuIn}(\text{S},\text{Se})_2$ (CISSe) are particularly interesting as the bandgap can be tuned by changing the elemental $x = [\text{S}]/[\text{S} + \text{Se}]$ composition of the absorber (1.04 eV for $x = 0$, and 1.53 eV for $x = 1$).^[4] Furthermore, high absorption coefficients of CISSe permit solar cells with thin film PV absorbers, which can be fabricated by nonvacuum-based ink-deposition routes (IDR).^[5] IDRs are scalable, inherently low cost, and allow high throughput manufacturing with high material utilization, offering an intriguing alternative to vacuum-based deposition processes.^[1,6]

Currently, the highest efficiency CISSe PV devices up to 19.2% are fabricated by coevaporation process.^[7] There, in the commonly employed three-stage process,

1. Introduction


Widescale implementation of photovoltaic (PV) technologies hinges on the interplay between power conversion efficiencies (PCEs), operational stability, and manufacturing costs.^[1] Combining two or more solar cells with different bandgaps (the highest on the sun-facing side) in a tandem configuration effectively utilizes a wider range of the solar spectrum, and can boost device efficiencies by over 40%.^[2] For example, high

the absorber transitions from Cu-poor ($[\text{Cu}]/[\text{In}] < 1$) to Cu-rich ($[\text{Cu}]/[\text{In}] > 1$) compositions, and back to Cu-poor to maintain an overall Cu-deficient film composition ($[\text{Cu}]/[\text{In}] \approx 0.95$).^[6] The Cu-poor/Cu-rich transition is accompanied by structural and morphological changes that include an increase in grain size, recrystallization (stress relaxation), and a decrease in stacking fault density and planar defects.^[8] In 2019, Feurer et al. reported that Urbach energies decreased from ≈ 20 to 16 meV by increasing the Cu concentration in the absorber films (from $[\text{Cu}]/[\text{In}] \approx 0.88$ to 0.95).⁷ Record PCEs of 19.2% were demonstrated for CISSe devices with a near stoichiometric absorber composition, having an external quantum efficiency (EQE) determined minimum bandgap (E_g) of 1.0 eV. Notably, however, in terms of film processing, the absorber growth process for vacuum- and IDR-based absorbers is fundamentally different, i.e., a single-step deposition (elemental evaporation rates and substrate temperature are adjusted to tailor grain growth and bandgap gradients) versus two-step process (nearly all the constituent elements (Cu, In, and S/Se) mixed in atomic compositions, deposited, and thermally treated in a chalcogen environment for grain growth). For this reason, more research needs to be carried out to use inks with controlled stoichiometry and optimized heat treatment processes to facilitate grain growth, reduce residual impurities, film porosity, and improve film morphology.^[9]

Herein, an *N,N*-dimethylformamide (DMF)–thiourea (TU)-based molecular IDR is presented for the fabrication of narrow-bandgap (≈ 1.0 eV) CISSe PV absorber layers. We report

S. Suresh, T. H. Chowdhury, A. R. Uhl
Laboratory for Solar Energy & Fuels (LSEF)
School of Engineering
The University of British Columbia
Kelowna V1V 1V7, Canada
E-mail: alexander.uhl@ubc.ca

D. Abou-Ras
Helmholtz-Zentrum Berlin für Materialien und Energie GmbH
14109 Berlin, Germany

 The ORCID identification number(s) for the author(s) of this article can be found under <https://doi.org/10.1002/solr.202300437>.

© 2023 The Authors. Solar RRL published by Wiley-VCH GmbH. This is an open access article under the terms of the Creative Commons Attribution-NonCommercial-NoDerivs License, which permits use and distribution in any medium, provided the original work is properly cited, the use is non-commercial and no modifications or adaptations are made.

DOI: 10.1002/solr.202300437

the influence of Cu content on phase formation, morphology, optoelectronic properties, and device performance. Conductive Cu_{2-x}Se phases were observed at both the surface and bulk of Cu-rich films, resulting in the deterioration of device performance. KCN or ammonium sulfide ($\text{NH}_4)_2\text{S}$, AS) solutions (LD50:rat- $5^{[10]}$ and 350 mg kg^{-1} ,^[11] respectively) were used to remove the conductive and detrimental Cu_{2-x}Se phases. Subsequently, devices with stoichiometric absorber films demonstrated improved photoluminescence (PL), an effective minority lifetime (τ) of $\approx 6 \text{ ns}$, open-circuit voltage (V_{OC}) of 526.1 mV, and active area efficiencies of up to 13.2% without antireflection (AR) coating.

2. Results and Discussion

Molecular ink precursor solutions were prepared by adding TU, Cu(I)Cl, and In(III)Cl to DMF solvent in the sequence mentioned and stirred until complete dissolution before adding the next reagent.^[12] Molecular inks with varying [Cu]/[In] ratios (0.85, 1.0, and 1.15) were used to prepare the Cu-poor, stoichiometric, and Cu-rich precursor films, respectively (experimental details in Supporting Information). KCN (10 wt% in H_2O , 60 s) or ammonium sulfide (28 wt% in H_2O , 600 s) treatments were used to remove potential phases from the film surface. For simplicity, CISSe films fabricated under Cu-poor, stoichiometric, and Cu-rich conditions are denoted by their composition, in combination with the etchant used. For example, the Cu-rich, KCN-treated samples are denoted by 1.15 (K), and the untreated samples are denoted by 1.15 (U).

Figure 1 shows the top view scanning electron microscopy (SEM) images of the untreated, and AS- or KCN-treated

CISSe films with varied [Cu]/[In] ratios. Cu-poor films exhibited small polyhedral/triangular shaped grains with irregular grain boundaries (GBs) (Figure 1a), which resulted in a rough surface (root mean square [rms] roughness $\approx 80 \text{ nm}$, as determined by profilometry measurements). Comparatively, stoichiometric and Cu-rich absorber layers exhibited significantly larger grains (see Figure 1b,c), consistent with reported Cu_{2-x}Se liquid phases during selenization that can provide a capillary force to merge small grains through Ostwald ripening.^[13] KCN, or AS postseleznization treatments were used to selectively remove the surface Cu_{2-x}Se precipitates. As further shown in Figure 1b,c, the surface Cu_{2-x}Se precipitates could successfully be removed using either etchant solution. Notably, 60 s of KCN treatment was sufficient for Cu_{2-x}Se removal from film surface, while 600 s of AS treatment was required to effectively remove the Cu_{2-x}Se precipitates from absorber film surface (see Figure S1, Supporting Information). Buffière et al. attributed the difference in the removal rates to the higher stability constant of the resulting Cu complex formed with KCN when compared to AS.^[14] Notably, the surface of the 1.15 (AS, K) films (Figure 1b,c) appeared to be dimpled on account of the removal of large-grained Cu_{2-x}Se precipitates ($> 3 \mu\text{m}^2$), while no such dimples were detected at the surface of 1.0 (AS, K) absorber films.

Energy dispersive X-Ray spectroscopy (EDX) was conducted using accelerating voltages of 7 and 20 kV to determine the compositional information of the absorber films at different depths. EDX values taken at 7 kV (beam interacts with the top $\approx 200 \text{ nm}$ of the film) confirmed the [Cu]/[In] composition of the untreated films around 0.86, 1.03, and 1.14 for Cu-poor, stoichiometric, and Cu-rich films, respectively (see Table S1, Supporting

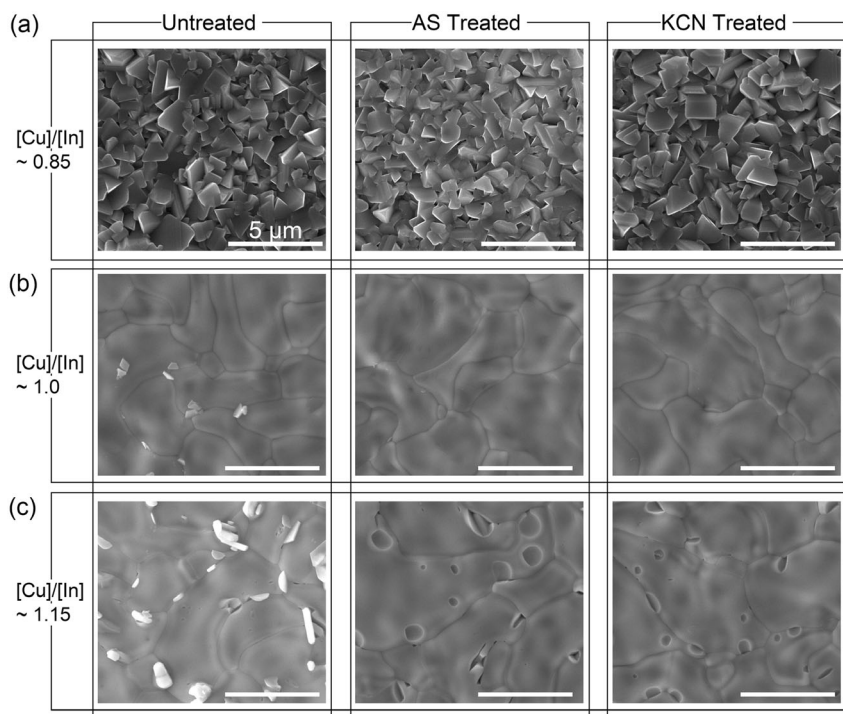


Figure 1. Top-view scanning electron microscope images of untreated, and AS or KCN Cu-poor (top row, a) stoichiometric (middle row, b) and Cu-rich films (bottom row, c), respectively.

Information), which is in good agreement with our ink composition and the accuracy of the measurement. Furthermore, EDX values indicated near-stoichiometric compositions ($[\text{Cu}]/[\text{In}] \approx 1.0$) for KCN- or AS-treated stoichiometric, and Cu-rich samples, suggesting sufficient Cu_{2-x}Se phase removal from the film surface, corroborating SEM results. However, EDX values taken at 20 kV (information depth around $\approx 1 \mu\text{m}^{[15]}$) showed that the $[\text{Cu}]/[\text{In}]$ ratios exceeded 1.0 for both KCN- and AS-treated Cu-rich absorber films (see Table S1, Supporting Information). This indicates remnant Cu_{2-x}Se in absorber layer bulk, which could not be removed with either KCN or AS surface treatments. Further, all films showed low sulfur content with $[\text{S}]/[\text{S}] + [\text{Se}]$ ratios varying from 0.01 (stoichiometric), to 0.05 (Cu-poor), to 0.08 (Cu-rich), revealing sufficient selenization.

X-Ray diffraction (XRD) data of all absorbers showed characteristic CISSe reflections ((112), (220/204), and (312), not shown here).^[16] Figure 2a shows the (112) reflection of the untreated, and KCN- or AS-treated absorber films with varying $[\text{Cu}]/[\text{In}]$ ratios. A (112) peak shift to lower reflection angles can be attributed to the substitution of sulfur with selenium after film selenization (from 27.86 for pure CuInS_2 , JCPDS 65-2732 to 26.73 for pure CuInSe_2 , JCPDS 87-2265). The (112) reflection at 26.75 (Figure 2a) for the 1.0 (U) and 1.0 (K) absorbers confirmed the low sulfur incorporation of $<5.0\%$ in the films, corroborating EDX results.

A shoulder was detected at the high-angle side of the main (112) reflection for 1.0 (U) and 1.15 (U), attributed to Cu_{2-x}Se (PDF 04-014-3323).^[17] Accordingly, the shoulder disappeared after KCN or AS treatment for both the 1.0 and 1.15 absorber compositions, suggesting the selective removal of Cu_{2-x}Se phases from the absorber films. Notably, it appears that AS-etched films with $[\text{Cu}]/[\text{In}]$ ratios ≥ 1 show a slight shift of the (112) reflection toward higher diffraction angles. This could be related to an AS-mediated sulfur incorporation into the absorber.^[14] Further studies in this direction are ongoing. Furthermore, we note that the $I(112)/I(204)/I(220)$ aspect ratios for absorber films used in this study were about ≈ 2.65 , irrespective of their chemical composition, which suggested that the films also did not exhibit a significantly preferred crystal orientation.^[18] For comparison, $I(112)/I(204)/I(220) = 2.5$ (ICPDS 40-1487) in randomly oriented CuInSe_2 (CISe) films.

Raman spectra (Figure 2b) showed that the CISSe films exhibited characteristic A_1 ($173\text{--}177 \text{ cm}^{-1}$) vibrational mode, which corresponds to the motion of the anions (Se and S) with the cations (Cu and In) at rest.^[19,20] Besides, minor peaks at $\approx 210 \text{ cm}^{-1}$ (E mode, all the samples) and $\approx 228 \text{ cm}^{-1}$ (B₂/E mode, stoichiometric) were detected.^[19,21] Notably, the A_1 band appears stronger in the Cu-poor ($\approx 175 \text{ cm}^{-1}$) and Cu-rich ($\approx 176 \text{ cm}^{-1}$) films than in stoichiometric samples ($\approx 174 \text{ cm}^{-1}$), due to the relatively

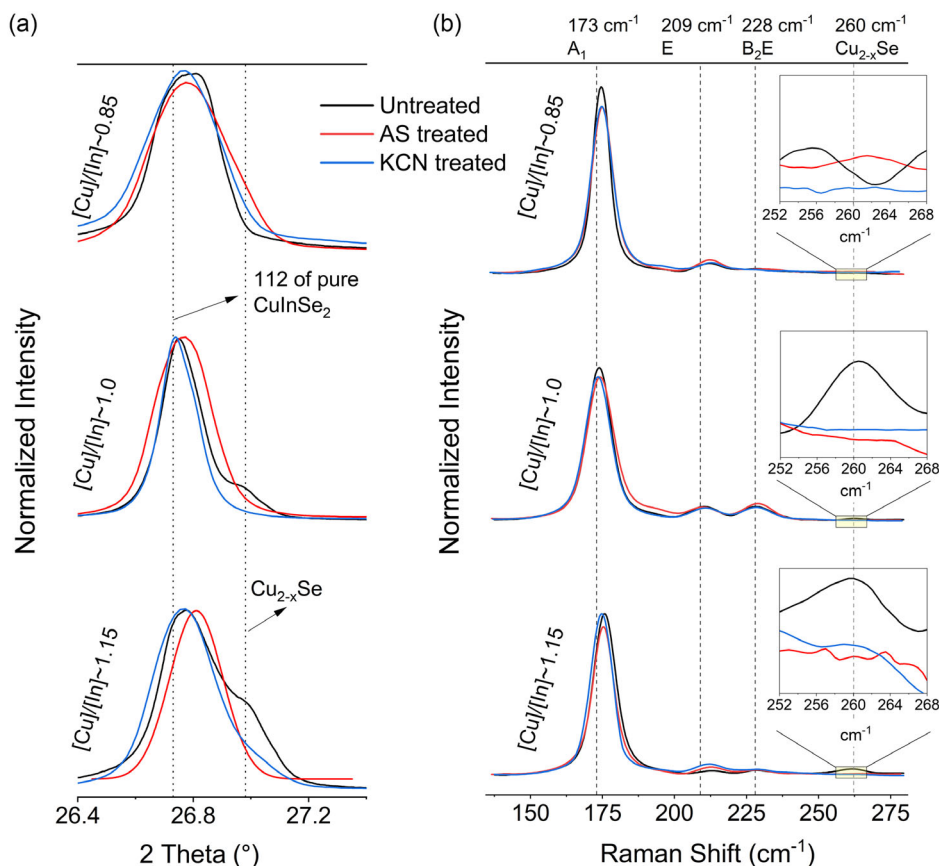


Figure 2. a) XRD reflection patterns of the untreated (black) and AS- (red) or KCN- (blue) treated absorber films. Shoulder peaks remnant of Cu_{2-x}Se (PDF 04-014-3323) were detected in the 1.0 (U), and 1.15 (U) films. The shoulder peaks disappeared after AS or KCN treatments. b) Raman spectra for untreated (black), and AS (red) or KCN (blue) treated absorber films. The inset enlarges Raman modes of Cu_{2-x}Se at 260 cm^{-1} detected in the untreated Cu-rich and stoichiometric films.

higher S-content in the respective absorber films (i.e., lower atomic mass of S with respect to Se).^[2,19]

Similar behavior was noted for the E and B₂/E modes, with the peak shift to higher wavenumbers (w.r.t. to stoichiometric CuInSe₂) being ascribed to the variation in [S]/[S] + [Se] content in absorber film surface.^[19–23] Furthermore, in addition to the A1 and E vibrational modes, peaks at $\approx 260\text{ cm}^{-1}$, corresponding to the A1 vibrational mode of Cu_{2–x}Se phases, were detected in the 1.0 (U) and 1.15 (U) samples (Figure 2b, inset).^[24] Consistent with XRD and SEM data, the Cu_{2–x}Se vibrational modes were not detected in the KCN- or AS-treated stoichiometric and Cu-rich films, suggesting the complete removal of the Cu_{2–x}Se phases from film surface.

To elucidate the grain microstructure of the untreated and KCN- or AS-treated stoichiometric and Cu-rich CISSe layers, electron backscatter diffraction (EBSD) maps were collected in top-view configuration (see Figure 3). The CISSe phases are depicted in red, Cu₂Se phases are depicted in blue, GBs in black, and unidentified phases in white. The phase distribution maps extracted from the EBSD data (see Figure 3a,b) show that Cu₂Se phases are detected for both film compositions (stoichiometric and Cu-rich).

Furthermore, the Cu₂Se binary phases were predominantly found at the GBs, confirming the SEM results (see Figure 1b,c). Notably, CISSe layers exhibited significant area fractions of Cu₂Se phases, even for the surface-treated devices. Furthermore, the area fractions of Cu₂Se decreased after both AS and KCN surface treatments to a similar extent, independent of the reagent used (see Table 1). Importantly, for the surface treated devices, Cu₂Se grains were not detected in top-view SEM and EDX characterization, but their detection by EBSD at 20 keV (with information depth of $\approx 1\ \mu\text{m}$) suggests the formation of binaries in the bulk—in agreement to 20 keV EDX. Further, no preferred orientations were detected for any CISSe absorber layers (see Figure S2, Supporting Information, for disorientation angle distributions), corroborating the XRD results. Also, from the EBSD data, the average grain size of the 1.0 (U) and 1.15 (U) films was determined to ≈ 2.5 and $4.4\ \mu\text{m}$, respectively. This result is consistent with studies that have shown that Cu₂Se formed inside the bulk of a Cu-rich CISSe absorber layer may not be removed.^[9]

Table 1. EBSD-determined real phase fractions of CISe and Cu₂Se phases.

Phase	1.0	1.0 [AS]	1.0 [K]	1.15	1.15 [AS]	1.15 [K]
CISe	92	94	96	91	94	95
Cu ₂ Se	4.7	3.1	3.3	6.4	4.4	2.3
Zero solutions	3.3	2.9	0.7	2.6	1.6	2.7
Cu ₂ Se/CISe	5.1	3.3	3.4	7.0	4.7	2.4

Minority carrier lifetime measurements were conducted on CdS-coated KCN-etched absorbers (see Figure 4a). All samples showed characteristic biexponential PL decays with varying time scales. KCN-treated stoichiometric absorbers showed significantly longer lifetimes ($\tau_{\text{avg}} = 6\text{ ns}$, following method in ref. [25]) when compared with Cu-poor absorber layers ($\tau_{\text{avg}} = 3\text{ ns}$) and Cu-rich absorbers ($\tau_{\text{avg}} = 1\text{ ns}$). In addition, a twofold and fourfold increase in the PL peak intensity was measured for the stoichiometric film (see Figure 4b) when compared with its Cu-poor and Cu-rich counterpart, respectively, suggesting superior material quality for the stoichiometric films. Measurements of the charge carrier density and width of the space charge region were conducted by capacitance–voltage profiling (C–V). The apparent doping concentration was extracted from the C–V measurements using methods mentioned in ref.[26] as shown in Figure 4c. By increasing the [Cu]/[In] ratio from 0.85 to 1.0, the carrier densities and space charge region (SCR) widths (wd) are reduced and increased, respectively. The highest charge carrier densities of $9.1 \times 10^{15}\text{ cm}^{-3}$ were obtained for the 0.85 (K) devices, compared to the $\approx 6.6 \times 10^{15}\text{ cm}^{-3}$ for both the 1.0 (K) and 1.15 (K). Furthermore, the SCR was wider in the 1.0 (K) device ($\approx 263\text{ nm}$) than that of the 0.85 (K) and 1.15 (K) device (≈ 250 and $\approx 249\text{ nm}$, respectively). Besides, the 1.0 (K) and 1.15 (K) samples showed similar doping profiles, with additional Cu_{2–x}Se phases not affecting the defect concentrations in the bulk absorber film.^[27] EQE measurements were conducted on select high-efficiency devices, to corroborate absorber bandgap and short-circuit current values. The bandgap energies were estimated as 1.05, 1.01, and 1.04 eV for 0.85 (K),

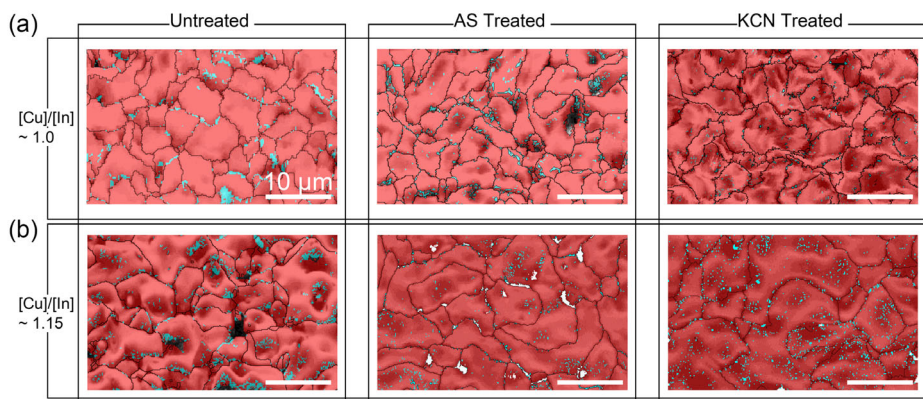


Figure 3. Plan-view EBSD phase-distribution maps (CISe phase – red, and Cu₂Se phase – blue) of a) untreated, AS or KCN treated, stoichiometric films, and b) untreated, AS or KCN treated Cu-rich films respectively.

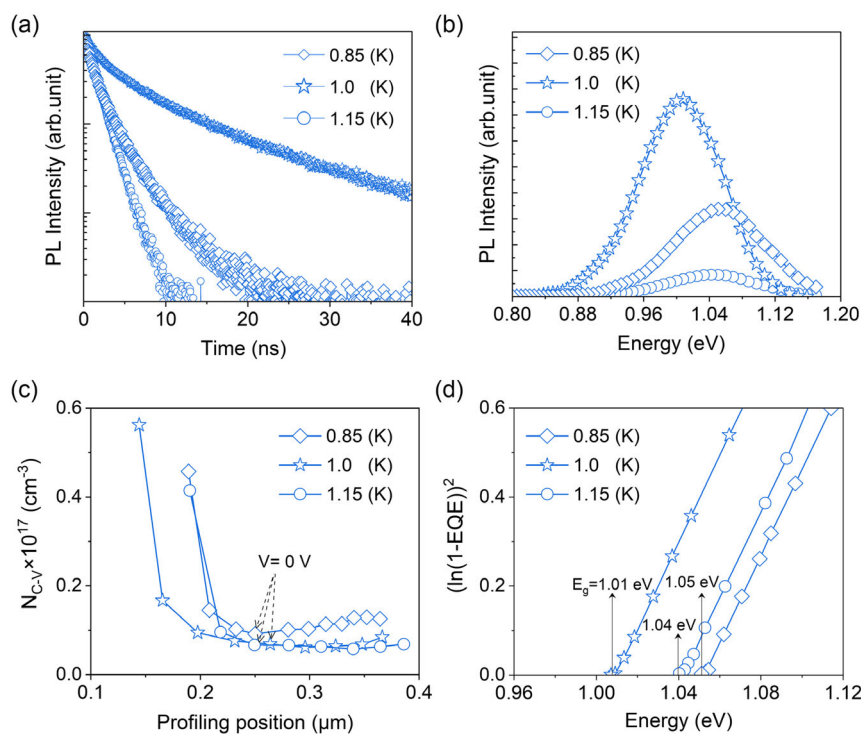


Figure 4. a) Time resolved photoluminescence (TRPL) data for CdS-coated, 0.85 (K), 1.0 (K), and 1.15 (K) samples, respectively. Considering the absorption coefficient of the CISSe layer the penetration depth of the laser was estimated at ≈ 80 nm, suggesting laser-generated carriers were primarily located in the depletion region. b) Photoluminescence spectra of KCN-treated, CdS-coated absorber films with varying Cu content. c) Comparison of depth profiles of apparent doping density (N_{CV}) extracted from C–V measurements for KCN-treated, CdS-coated absorber films with varying Cu content. d) Extraction of minimum bandgaps from EQE for completed solar cell devices.

1.0 (K), and 1.15 (K) films, respectively (see Figure 4d). Subsequently, the low band energies of the absorber films, close to that of pure CuInSe_2 (≈ 1.0 eV), demonstrated near-complete sulfur substitution by selenium (from precursor to absorber). This corroborates the PL data showing emission peaks at 1.05, 1.0, and 1.04 eV for 0.85 (K), 1.0 (K), and 1.15 (K).

Solar cell devices were fabricated in a typical cell architecture (Mo/CISSe/CdS/i-ZnO/ITO/Ni/Al), and subsequently characterized by current density–voltage (J – V) measurements. The average device parameters, including short-circuit current density (J_{SC}), V_{OC} , fill factor (FF), and PCE, are summarized in Table 2. Unless otherwise stated, the J – V curves and power conversion efficiencies are based on active area. By increasing the [Cu]/[In] ratio from 0.85 to 1.0, the average PCE of untreated devices increased from 10.1% to 10.6%, with the main enhancement gained from higher V_{OC} s (from 495 to 521 mV). Further increases in the [Cu]/[In] ratio (i.e., 1.15 (U) device) decreased the average PCEs to around 4.4%, with the low shunt resistance (R_{sh} , $\approx 0.2 \text{ k}\Omega \text{ cm}^2$) and FF ($\approx 42.8\%$), suggesting remnant highly conductive Cu_{2-x}Se phases at the surface and/or in the bulk of the absorber layer. As Cu_{2-x}Se was progressively removed from the surface of the Cu-rich samples (using KCN or AS), the electrical behavior of the solar cell improved (see Table 2).

Subsequently, higher shunt resistances (≈ 0.7 and $\approx 0.8 \text{ k}\Omega \text{ cm}^2$), lower series resistances (≈ 1.7 and $1.8 \text{ }\Omega \text{ cm}^2$), and FFs (see Table 2) allowed for average PCEs of about 10.3% and 9.8% for the 1.15 (K) and 1.15 (AS), respectively.

Table 2. Summary of active area device parameters of the CISSe solar cells (avg. of 15 devices) with the absorbers fabricated from Cu-poor, stoichiometric, and Cu-rich molecular precursor inks, respectively.

Device	J_{SC}	V_{OC}	FF	PCE	R_{shunt}	R_{series}
	[mA cm^{-2}]	[mV]	[%]	[%]	[$\text{k}\Omega \text{ cm}^2$]	[$\Omega \text{ cm}^2$]
0.85 [U]	33.4 ± 0.3	495 ± 2	61.3 ± 0.6	10.1 ± 0.1	1.1 ± 0.2	1.9 ± 0.1
0.85 [K]	34.6 ± 0.1	504 ± 1	62.5 ± 0.3	10.9 ± 0.1	1.4 ± 0.1	1.2 ± 0.2
0.85 [AS]	34.4 ± 0.2	505 ± 1	62.1 ± 0.5	10.8 ± 0.1	1.5 ± 0.1	1.3 ± 0.2
1.0 [U]	33.4 ± 0.3	521 ± 2	61.3 ± 0.4	10.6 ± 0.1	2.2 ± 0.2	1.1 ± 0.1
1.0 [K]	36.8 ± 0.4	524 ± 2	66.1 ± 0.5	12.8 ± 0.2	2.5 ± 0.1	0.4 ± 0.1
1.0 [AS]	37.1 ± 0.3	522 ± 4	64.9 ± 0.8	12.6 ± 0.2	2.4 ± 0.1	0.5 ± 0.1
1.15 [U]	24.9 ± 2	414 ± 7	42.8 ± 3	4.4 ± 0.2	0.2 ± 0.1	4.1 ± 0.4
1.15 [K]	34.2 ± 0.7	487 ± 1	61.0 ± 1	10.2 ± 0.3	0.7 ± 0.3	1.7 ± 0.1
1.15 [AS]	33.0 ± 0.9	488 ± 6	60.8 ± 1	9.8 ± 0.2	0.8 ± 0.2	1.8 ± 0.1

Notably, all the surface-treated devices (including Cu-poor samples) outperformed baseline devices of their respective film compositions, suggesting beneficial surface modifications beyond Cu_{2-x}Se removal. KCN may act as a potassium source with benefits similar to K postdeposition treatments,^[28] while AS treatments may lead to sulfur substitution at the film surface.^[14] Increased sulfur toward the absorber surface may decrease the conduction band offset toward the buffer layer,

thereby enabling efficient charge collection and higher FF values.^[29] For the 1.0 (K) devices, higher FF (from 61.3% to 66.1%) and J_{SC} (from 33.4 to 36.8 mA cm⁻²) led to average PCEs of 12.8%. Average PCEs of 10.9% were obtained by the 0.85 (K) devices, an 8% (abs.) increase when compared to the 0.85 (U) devices. For the 0.85 (AS) and 1.0 (AS) devices, the FF improved from 61.1% and 61.3% to 62.2% and 64.9%, respectively. Combined with the improvements to the J_{SC} , the PCE increased from 10.1% to 10.8% and from 10.6% to 12.6%, respectively, for devices with the AS-treated Cu-poor and stoichiometric absorber layers.

Figure 5a-c shows the $J-V$ curves of the best-performing PV devices with varying copper content.^[9] We report a highest PCE of 13.2%, obtained by a 1.0 (K) device having a J_{SC} , V_{OC} , and FF of 36.3 mA cm⁻², 526.1 mV, and 69.1%, respectively. KCN-treated, Cu-poor devices, demonstrated a highest PCE of 11.6%, J_{SC} of 34.6 mA cm⁻², V_{OC} of 507.4 mV, and FF of 66.1%. Compared to the 1.0 (K), the highest efficiency 1.15 (K) ($\approx 10.8\%$) device had 8.2% (abs.) lower V_{OC} , followed by FF (6.9% deficiency) and J_{SC} (5.2% deficiency).

The improvement in the electrical characteristics of the 1.0 (K) and 0.85 (K) devices can be attributed to higher carrier lifetimes (see Figure 4a), superior film quality (fourfold increase in PL response, Figure 4b), smoother absorber surfaces, and the lack of surface dimples after film treatment (see Figure 1c). Further, the external quantum efficiency data for the highest efficiency devices with varying Cu ratios are shown in Figure 4d. The overall increase in the spectral response (600–1200 nm wavelength range) for devices with [Cu]/[In] ≈ 1.15 , to 0.85, to 1.0, is in line with increased minority carrier lifetimes and SCR width from

TRPL and $C-V$ measurements, respectively, indicating improved carrier collection. Calculated J_{SC} values from EQE were 34.1, 35.5, and 33.7 mA cm⁻² for the 0.85 (K), 1.0 (K), and 1.15 (K) device, respectively, consistent with the $J-V$ results. Notably, our champion V_{OC} of 526.1 mV exceeds values of the currently reported highest efficient DMF-TU-based device (active area PCE $\approx 14.5\%$, 38.5 mA cm⁻² J_{SC} , 520 mV V_{OC} , 73% FF, with MgF₂) with similar bandgaps ($E_g = 1.01$ eV), indicating excellent material quality.^[9] Further improvements are expected from additional layer optimizations (e.g., bandgap gradients, alkali postdeposition treatments,^[30,31] surface passivation^[32,33]) and application of MgF₂ AR coatings.

3. Conclusion

In conclusion, it was shown that the [Cu]/[In] ink stoichiometry in IDRs can affect a myriad of parameters including the grain size, roughness, phase purity, minority carrier lifetime, charge carrier concentration and depletion width, and ultimately device performance. Cu-poor stoichiometries ([Cu]/[In] < 1) lead to roughest film surfaces (rms roughness > 20 nm) and smallest grain sizes (< 400 nm), while near stoichiometric ink compositions ([Cu]/[In] ≈ 1) yielded large-grained ($\approx 2 \mu\text{m}$) absorber layers with smooth absorber surfaces (rms roughness < 20 nm, see Figure S3, Supporting Information). XRD, Raman, and SEM measurements confirmed that KCN and AS surface treatments selectively removed remnant Cu_{2-x}Se phases from the film surface, while EBSD and depth-dependent EDX indicated remnant Cu_{2-x}Se in the bulk absorber layer, particularly for Cu-rich compositions.

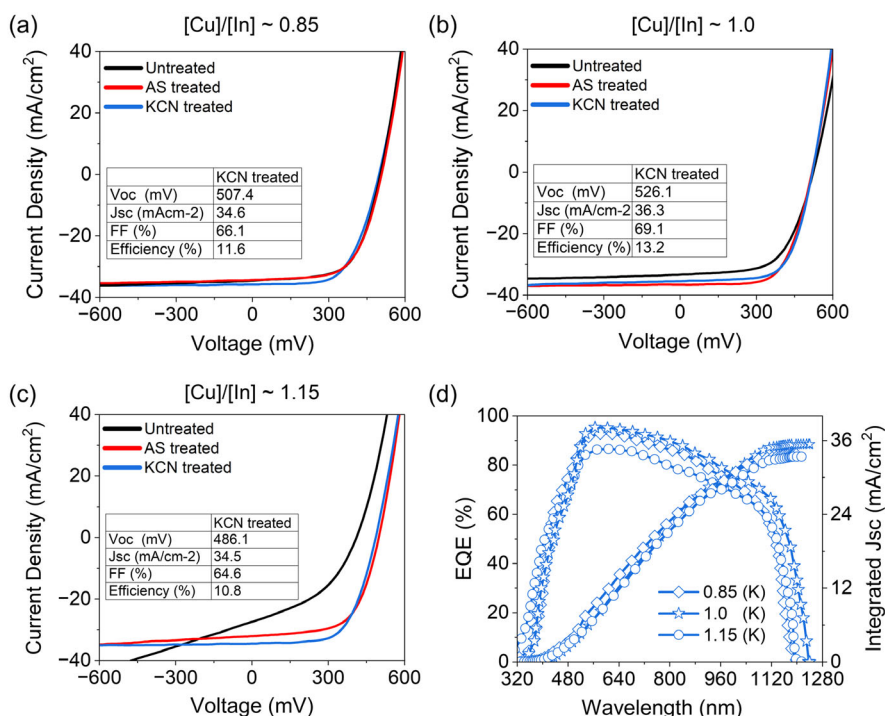


Figure 5. a–c) $J-V$ characteristics of the best performing untreated (black), AS (red) or KCN (blue) treated devices with varying [Cu]/[In] ratios. The inset table in the respective figures provide the electrical performance data of the champion device for the respective film compositions (active area, all KCN treated). d) EQE measurements of the respective champion devices alongside integrated current densities.

Thus, by carefully tailoring the absorber film composition and optimizing surface treatments processes, active area efficiencies of 13.2% (without MgF₂) were obtained for low-bandgap (1.01 eV) CISSe devices with high open-circuit voltages up to 526.1 mV.

Supporting Information

Supporting Information is available from the Wiley Online Library or from the author.

Acknowledgements

The authors would like to acknowledge that this work was conducted on the traditional, ancestral, and unceded territory of the Syilx Okanagan Nation (Kelowna). S.S., T.H.C., and A.R.U. acknowledge the financial support provided by the Natural Sciences and Engineering Research Council of Canada (NSERC), through grants RGPIN-2019-05489 and DGEER-2019-00450 as well as the Canada Foundation for Innovation (CFI) and the British Columbia Knowledge Development Fund (BCKDF) through grants 39081 and 42549. A.R.U. further acknowledges funding through the UBC Okanagan Principal's Research Chair (Tier 2). D.A. is grateful for support by the BMWK-funded project EFFCIS-II (03EE1059B) and by the German-Israeli Helmholtz International Research School HI-SCORE (HIRS-0008). Ghanshyam Chandrashekar is acknowledged for PL and EQE measurements.

Conflict of Interest

The authors declare no conflict of interest.

Data Availability Statement

The data that support the findings of this study are available from the corresponding author upon reasonable request.

Keywords

chalcogenides, CIS, non-vacuum, photovoltaics, solar cells

Received: June 16, 2023
Published online: July 5, 2023

- [1] S. Suresh, A. R. Uhl, *Adv. Energy Mater.* **2021**, *11*, 2003743.
- [2] A. D. Vos, *J. Phys. D Appl. Phys.* **1980**, *13*, 839.
- [3] S. P. Bremner, M. Y. Levy, C. B. Honsberg, *Progr. Photovolt. Res. Appl.* **2008**, *16*, 225.
- [4] R. Félix, A. Weber, O. Zander, H. Rodriguez-Álvarez, B.-A. Schubert, J. Klaer, R. G. Wilks, H.-W. Schock, R. Mainz, M. Bär, *J. Mater. Chem. A* **2019**, *7*, 2087.
- [5] B. M. Basol, *Electrochem. Solid-State Lett.* **1999**, *1*, 252.
- [6] S. Suresh, D. J. Rokke, A. A. Drew, E. Alruqobah, R. Agrawal, A. R. Uhl, *Adv. Energy Mater.* **2022**, *12*, 2103961.
- [7] T. Feurer, R. Carron, G. Torres Sevilla, F. Fu, S. Pisoni, Y. E. Romanyuk, S. Buecheler, A. N. Tiwari, *Adv. Energy Mater.* **2019**, *9*, 1901428.
- [8] C. Li, E. S. Sanli, D. Barragan-Yani, H. Stange, M.-D. Heinemann, D. Greiner, W. Sigle, R. Mainz, K. Albe, D. Abou-Ras, et al., *Phys. Rev. Lett.* **2020**, *124*, 095702.
- [9] J. Jiang, R. Giridharagopal, E. Jedlicka, K. Sun, S. Yu, S. Wu, Y. Gong, W. Yan, D. S. Ginger, M. A. Green, X. Hao, W. Huang, H. Xin, *Nano Energy* **2020**, *69*, 104438.
- [10] Ammonium Sulfide Solution; CAS RN: 12135-76-1; rev. 1, Tessenderlo Kerley, Inc., Phoenix, AZ **2021**, <https://www.moleko.com/sites/moleko/files/files/2021-10/Ammonium%20sulfide%20solution%20SDS.pdf> (Accessed: October 2023).
- [11] M. Sheehy, J. L. Way, *J. Pharmacol. Exp. Ther.* **1968**, *161*, 163.
- [12] A. R. Uhl, A. Rajagopal, J. A. Clark, A. Murray, T. Feurer, S. Buecheler, A. K. Y. Jen, H. W. Hillhouse, *Adv. Energy Mater.* **2018**, *8*, 1801254.
- [13] R. M. German, P. Suri, S. J. Park, *J. Mater. Sci.* **2009**, *44*, 1.
- [14] M. Buffière, A.-A. E. Mel, N. Lenaers, G. Brammertz, A. E. Zaghi, M. Meuris, J. Poortmans, *Adv. Energy Mater.* **2015**, *5*, 1401689.
- [15] C. Kameni Boumenou, A. Elizabeth, F. Babbe, A. Debot, H. Mönig, A. Redinger, *Progr. Photovolt. Res. Appl.* **2021**, *29*, 775.
- [16] T. Wada, N. Kohara, S. Nishiwaki, T. Negami, *Thin Solid Films* **2001**, *387*, 118.
- [17] J. A. Clark, A. Murray, J.-M. Lee, T. S. Autrey, A. D. Collord, H. W. Hillhouse, *J. Am. Chem. Soc.* **2019**, *141*, 298.
- [18] M. A. Contreras, M. J. Romero, R. Noufi, *Thin Solid Films* **2006**, *511–512*, 51.
- [19] J. Álvarez-García, B. Barcones, A. Pérez-Rodríguez, A. Romano-Rodríguez, J. R. Morante, A. Janotti, S.-H. Wei, R. Scheer, *Phys. Rev. B* **2005**, *71*, 054303.
- [20] C. Rincón, F. J. Ramírez, *J. Appl. Phys.* **1992**, *72*, 4321.
- [21] T. Schmid, N. Schäfer, S. Levchenko, T. Rissom, D. Abou-Ras, *Sci. Rep.* **2015**, *5*, 18410.
- [22] J. Álvarez-García, V. Izquierdo-Roca, P. Pistor, T. Schmid, A. Pérez-Rodríguez, *Sol. Cells* **2016**, *469*.
- [23] R. Bacewicz, W. Gebicki, J. Filipowicz, *J. Phys. Condens. Matter* **1994**, *6*, L777.
- [24] L. Sun, J. Ma, N. Yao, Z. Huang, J. Chu, *J. Mater. Sci. Mater. Electron.* **2016**, *27*, 9124.
- [25] B. Ohnesorge, R. Weigand, G. Bacher, A. Forchel, W. Riedl, F. H. Karg, *Appl. Phys. Lett.* **1998**, *73*, 1224.
- [26] J. T. Heath, J. D. Cohen, W. N. Shafarman, *J. Appl. Phys.* **2004**, *95*, 1000.
- [27] S. S. Hegedus, W. N. Shafarman, *Progr. Photovolt. Res. Appl.* **2004**, *12*, 155.
- [28] E. H. Alruqobah, R. Agrawal, *ACS Appl. Energy Mater.* **2020**, *3*, 4821.
- [29] S. Kim, M. S. Mina, J. Lee, J. Kim, *ACS Appl. Mater. Interfaces* **2019**, *11*, 45702.
- [30] C.-H. Chung, B. Lei, B. Bob, S.-H. Li, W. W. Hou, H.-S. Duan, Y. Yang, *Chem. Mater.* **2011**, *23*, 4941.
- [31] Y. Wang, S. Lv, Z. Li, *J. Mater. Sci. Technol.* **2022**, *96*, 179.
- [32] S. Suresh, J. de Wild, T. Kohl, D. G. Buldu, G. Brammertz, M. Meuris, J. Poortmans, O. Isabella, M. Zeman, B. Vermang, *Thin Solid Films* **2019**, *669*, 399.
- [33] S. Bose, J. M. V. Cunha, S. Suresh, J. De Wild, T. S. Lopes, J. R. S. Barbosa, R. Silva, J. Borme, P. A. Fernandes, B. Vermang, P. M. P. Salomé, *Sol. RRL* **2018**, *2*, 1800212.